Modified embedded-atom method potentials for the plasticity and fracture behaviors of unary fcc metals

Zachary H. Aitken,[1,*] Viacheslav Sorkin,[1] Zhi Gen Yu,[1] Shuai Chen,[1] Zhaoxuan Wu,[2] and Yong-Wei Zhang[1,†]
[1]*Institute of High Performance Computing, A*STAR, Singapore, Singapore 138632*
[2]*Department of Materials Science and Engineering, City University of Hong Kong, Hong Kong, China*

(Received 16 December 2020; revised 22 February 2021; accepted 1 March 2021; published 29 March 2021)

The predictability of molecular dynamics simulations on the plasticity and fracture behaviors of metals is critically dependent on the accuracy of the employed interatomic potential. Here we present an approach to fitting modified embedded-atom method (MEAM) interatomic potentials to several key properties obtained from first-principles calculations and literature data that govern the continuous mechanistic processes in pure unary fcc Ni, Al, and Cu metals. Along with the commonly used lattice and elastic properties, our MEAM potentials are fitted to the cohesive energy curve, the decohesive energy curve, and the generalized stacking fault energy curve, which are the key properties governing the lattice response to volumetric, fracture, and shear deformations. We further demonstrate that these potentials are able to accurately predict the experimental values for a range of other mechanically relevant properties. Importantly, the potentials presented here outperform all existing EAM/MEAM interatomic potentials readily available from the literature and thus enable more accurate simulations of plasticity and fracture behavior of unary fcc metals.

DOI: 10.1103/PhysRevB.103.094116

I. INTRODUCTION

Molecular dynamics (MD) simulation is an important tool for exploring the mechanical response of metals at the nanoscale [1–3]. Semiempirical potentials are advantageous for their ability to simulate large groups of atoms at longer timescales with a reasonable computational demand compared to first-principles simulations. A range of target properties, mainly including lattice, thermodynamic, and elastic properties, can be used to fit an interatomic potential. To model metallic systems, potentials built upon the embedded-atom method (EAM) [4,5] have been shown to be the most popular. Among the variants of EAM models, the modified embedded-atom method (MEAM) has proven to be the most flexible in representing metallic systems [6,7]. The MEAM differs from the original EAM in its inclusion of directionality when calculating the background electron density and explicitly accounting for screening between groups of atoms. The MEAM has been successful at modeling several unary fcc [8] and bcc [7] metallic systems as well as many alloy systems [9–11].

To fit an interatomic potential, common properties used as fitting targets include the lattice parameter and cohesive energy, lattice surface energies, vacancy formation energies, elastic constants, the bulk modulus, the pressure derivative of the bulk modulus, and the stable stacking fault energy. These are often calculated for a single reference lattice. The first difficulty for fitting involves choosing the set of target properties that best captures the intended applications of the potential. While there are many potentials that do well in capturing the elastic behavior of metals, how appropriate a conventional set of fitting target properties is for reproducing accurate plastic and fracture behaviors is questionable due to their complexity.

The second difficulty arises when attempting to employ a single data point to represent the fitting targets for applications that involve continuous processes. In general, the full reaction pathway of a continuous process cannot be accurately captured by a single data point. For example, the stacking fault energy from density functional theory (DFT) or the experimental value is often used to accurately fit the potential, which may be largely inaccurate to predict the full generalized stacking fault energy (GSFE) curve. To create a stacking fault, the system must pass through an energy barrier at the unstable stacking fault energy [Fig. 1(c)], and the slope of the stacking fault energy curve represents the force that the dislocation must overcome for nucleation or propagation. Therefore, it is the shape of the generalized stacking fault energy curve and not just the stacking fault energy that governs the dislocation nucleation and propagation behavior. The importance of the unstable stacking fault energy was noted in nanocrystalline simulations where the ratio of the unstable to stable stacking fault energies was shown to determine the nucleation of leading partial vs full dislocations [12]. A DFT-validated Mg MEAM potential that captured the full GSFE curves was used to explain the atomistic origin of high hardening and low ductility in Mg [2].

The inadequacy of fitting to a single data point has also been noted in simulations of planar fracture in Mg [13]. Interatomic potential parameters can easily be chosen to capture the surface energy of the fracture plane, which could be related to the fracture through the Griffith criteria [14].

*zach-aitken@ihpc.a-star.edu.sg
†zhangyw@ihpc.a-star.edu.sg

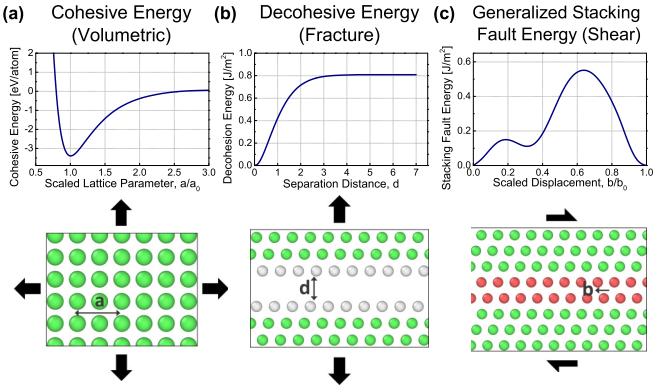

FIG. 1. Energy curves used as fitting targets for MEAM potentials. (a) shows the cohesive energy curve as a function of scaled lattice parameter and corresponds to volumetric deformation. (b) shows the decohesion energy curve as a function of separation distance and corresponds to fracture of atomic planes. (c) shows the generalized stacking fault energy curve as a function of scaled shear displacement and corresponds to shear deformation of atomic planes.

This approach ignores the continuous process of separating two atomic planes from their equilibrium separation to create two free surfaces, which often passes through the cutoff distance of the interatomic potential. If there is not a smooth decay of interaction before the cutoff radius, then approaching atoms can encounter anomalous forces that may either push the planes apart or act as a nonphysical restoring force [13].

These examples demonstrate that fitting interatomic potentials to single-valued properties can result in inaccurate or nonphysical behavior when considering continuous processes that are relevant for plastic deformation. It must then be important to fit to a wider range of properties and to the full energy curves that represent the atomic displacements present in continuous plastic processes. In this study, we present unary Ni, Al, and Cu MEAM potentials that can capture both conventional target material and mechanical properties as well as continuous-energy curves relevant for plastic deformation and fracture processes. Along with conventional fitting target properties, we include the cohesive energy curve, the decohesive energy curve, and the GSFE curve as targets. We demonstrate that our MEAM potentials outperform existing MEAM potentials from the literature in both the target fitting properties and predicted mechanical properties not included in the target property set.

II. METHODS

The targets for fitting include the equilibrium lattice parameter and cohesive energy; the {100}, {110}, and {111} surface energies; the cohesive energy curve; the decohesive energy curve; the generalized stacking fault energy curve; and the elastic constants. Target properties were calculated using first-principles methods in order to generate the target values and using MD during the fitting procedure. First-principles and MD simulations followed conventional methodologies previously described in the literature [15–23], and we encourage the reader to refer to the Supplemental Material [24] for details of the first-principles and MD simulation methodologies used to calculate these target properties.

For atomistic energy values, we choose to use the target values calculated from DFT. For bulk elastic constants, we find better agreement by using the reported experimental data. We find that this hybrid target approach provides better fits to both atomistic energies and bulk properties.

We omit a description of the MEAM formulation as it has been extensively covered elsewhere [6–9]; it suffices to say that our implementation employs the second-nearest neighbor formulation and provides for 15 adjustable parameters. To optimize this overdetermined system, we employ particle swarm optimization (PSO). Upper and lower limits for each adjustable parameter are assigned at the beginning of optimization, and particles are initialized by distribution throughout this bounded 15-dimensional parameter space. For each iteration of optimization, each particle performs MD simulations for each property using the Large-scale Atomic/Molecular Massively Parallel Simulator (LAMMPS) [25]. The error is calculated using the target data, and the objective function value is defined as a weighted squared sum error of all properties. PSO particle velocities and positions are updated based on the local and global minima, and optimization proceeds until no significant change in the objective function is observed. This typically corresponded to a decrease in the squared sum error of less than 5% but varied depending upon normalization conditions of the objective function. We have made several observations from these fittings that helped speed up the exploration of parameter space. Each parameter set is independent, which makes the PSO highly amenable to parallelization. The lattice parameter and cohesive energy were fundamental to all subsequent properties. After the equilibrium lattice parameter and cohesive energy for a given set of parameters were calculated, the error of these values was screened before we moved on to the remaining set of properties. If any calculated properties were above a threshold value, the PSO particle was assigned an arbitrarily large objective value, and the optimization algorithm moved on to the next particle. Some properties were observed to be coupled, and accurate fitting of one led to accurate fitting of others. For example, a strong weight of the relaxed {111} surface energy helped to fit the plateau value of the decohesion energy curve. As a result, error screening was also done on the relaxed surface energies. Parallelization and error screening of these properties significantly cut down on time required for fitting. Initial guesses for the Rose parameters used in calculating the pair potential term could easily be obtained prior to fitting by linear regression to the cohesive energy curve using the Rose energy function [26]. We also observed that including the gradient of the cohesive energy, decohesive energy, and GSFE curves in the calculations of errors could help in matching the correct shapes of these curves.

In order to compare our potentials against the literature, we performed the same set of computations for several readily available MEAM potentials. Most literature MEAM potentials were fit to standard thermodynamic and mechanical properties. For the Ni system, we chose the potentials in Refs. [27–30]. For the Al system, we chose [30–33]. For the Cu system, we chose [27,29,32,34].

TABLE I. MEAM parameters for our Ni, Al, and Cu potentials.

Element	E_c	r_e	α	β^0	β^1	β^2	β^3	t^1	t^2	t^3	A	$C_{\min}$	$C_{\max}$	d_{repuls}	d_{attrac}	r_c	Δr
Ni	4.850	2.478	4.823	2.000	1.267	2.321	3.122	1.159	−1.622	6.901	0.624	0.821	2.440	0.144	0.165	5.539	3.507
Al	3.427	2.8585	4.658	3.173	2.342	2.013	2.471	3.285	−0.057	5.194	1.024	0.350	2.539	0.043	0.063	6.500	2.586
Cu	3.533	2.561	5.150	3.984	3.000	6.347	1.948	4.039	2.866	1.000	0.860	0.390	2.771	0.080	0.030	6.406	3.316

III. FITTING RESULTS

The MEAM fitting parameters for our Ni, Al, and Cu potentials are given in Table I, and fitting targets for the cohesive energy, lattice parameter, surface energies, and elastic constants are summarized in Table II. We also provide the MEAM potential files formatted for LAMMPS in the Supplemental Material.

A. Ni target results

A summary of the fit error of target properties for our Ni MEAM potential are shown in Fig. 2 along with errors from the literature Ni MEAM potentials for comparison. Numerical values of these properties are given in Table S1. Our Ni MEAM potential captures the target surface energies well with absolute errors of −1.7%, 10.9%, and −4.6% for the {100}, {110}, and {111} surfaces, respectively. Our Ni MEAM potential also shows good reproduction of the elastic constants with absolute errors of 1.2%, −0.8%, and −4.6% for C_{11}, C_{12}, and C_{44}, respectively.

Figure 3 summarizes the target Ni cohesive energy, decohesive energy, and GSFE curves (target DFT data indicated by the solid curve) along with curves produced by our Ni MEAM potential (solid data points) and a comparison with the literature Ni MEAM potentials (open data points). As seen in Fig. 3(a), our Ni MEAM captures the target DFT cohesive energy curve and is fully continuous across the extent of the energy curve, avoiding discontinuities.

Figure 3(b) shows the target decohesive energy curve for Ni along with our fit Ni MEAM potential. Our Ni MEAM potential shows a good fit to the DFT target curve and is entirely smooth up to and including the plateau value where there is no interaction between the separated {111} planes. The plateau value, which represents the unrelaxed {111} surface energy of 1.86 J m^{-2}, is consistent with the computed relaxed {111} surface energy of 1.85 J m^{-2}.

As shown in Fig. 3(c), our Ni MEAM potential provides good agreement with the target DFT GSFE curve. The unstable and stable stacking fault energies produced by our Ni MEAM potential are 0.321 and 0.153 J m^{-2}, respectively, and these values compare well with the same values calculated from DFT of 0.333 and 0.193 J m^{-2}. Although typically not encountered in a physical simulation, our Ni MEAM potential is also able to capture the correct shape and magnitude of the second peak at $\frac{b}{b_0} \approx \frac{2}{3}$.

TABLE II. Target properties for our Ni, Al, and Cu potentials.

	Ni targets	Al targets	Cu targets
Lattice constant (Å)	3.505	4.042	3.622
Cohesive energy (eV)	−4.48	−3.427	−3.533
$E_{\{100\}}$ (J m^{-2})	2.37	0.94	1.49
$E_{\{110\}}$ (J m^{-2})	2.30	1.02	1.55
$E_{\{111\}}$ (J m^{-2})	1.94	0.81	1.32
C_{11} (GPa)	261.2	114.3	176.2
C_{12} (GPa)	150.8	61.9	124.9
C_{44} (GPa)	131.7	31.6	81.8

B. Al target results

A summary of the fit error of target properties for our Al MEAM potential is shown in Fig. 4 along with errors from the literature Al MEAM potentials for comparison. Numerical values of these properties are given in Table S2. Our Al MEAM potential captures the target surface energies well with absolute errors of 10.6%, 4.9%, and 0.0% for the {100}, {110}, and {111} surfaces, respectively. Our Al MEAM potential also shows good agreement with the elastic constants with absolute errors of 0.4%, 1.6%, and 0.0% for C_{11}, C_{12}, and C_{44} respectively.

Figure 5 summarizes the target Al cohesive energy, decohesive energy, and GSFE curves (target DFT data are indicated by the solid curve) along with curves produced by our MEAM potential (solid data points) and comparison with

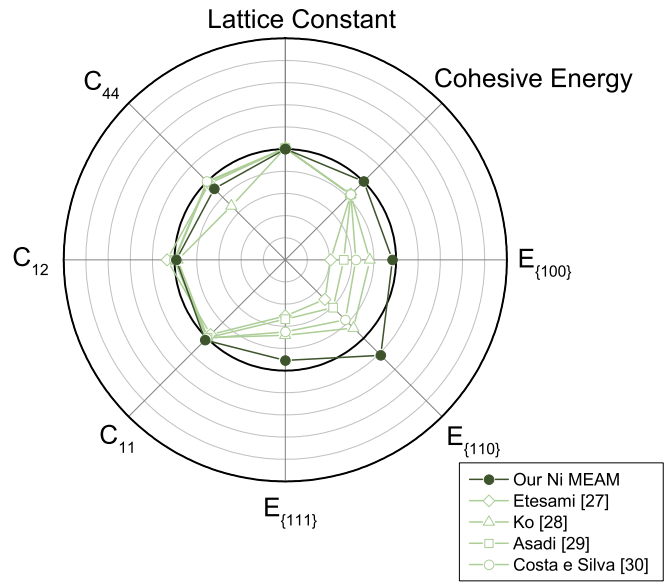

FIG. 2. Fitting error for the lattice constant, cohesive energy, surface energies, and elastic constants for our Ni MEAM potential and comparison Ni MEAM potentials from the literature. Circles are separated by 10% fitting error, where the thick inner circle indicates 0% error. Points closer to the center than the target indicate a negative error, whereas points farther from the center than the target indicate a positive error.

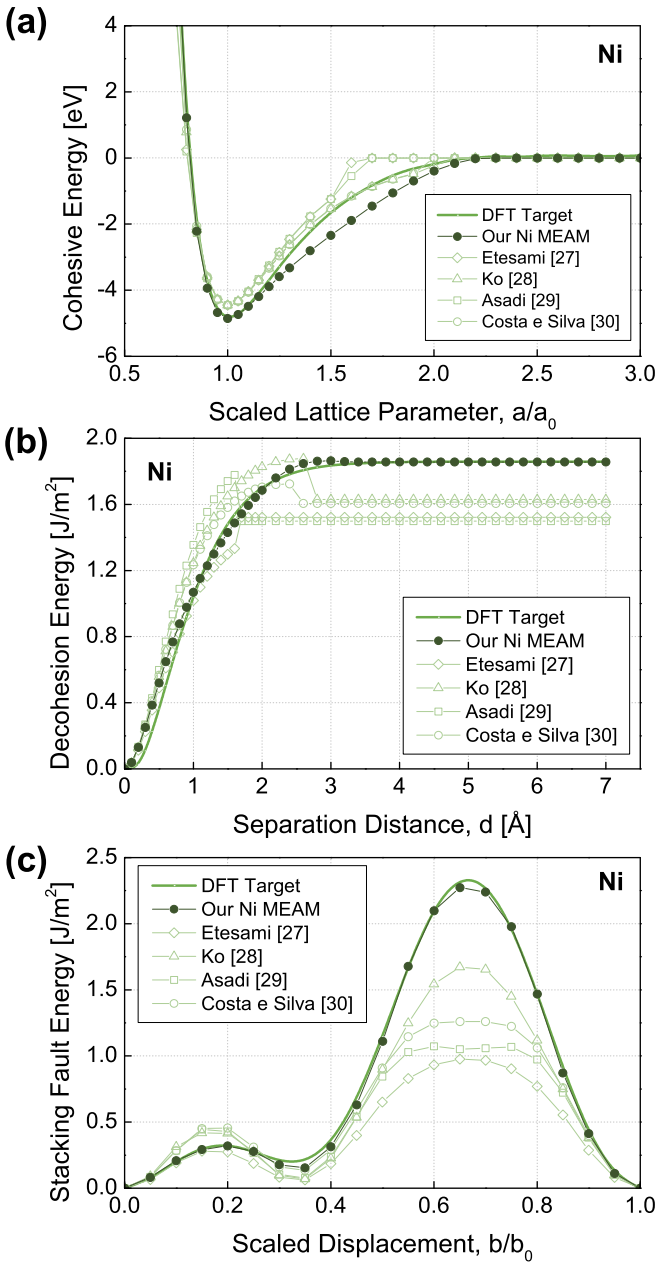

FIG. 3. Summary of target energy curves for Ni (solid curves) with our Ni MEAM potential (solid data points) and MEAM potentials from the literature (open data points). (a) shows the cohesive energy curve, (b) shows the decohesive energy curve, and (c) shows the GSFE curve.

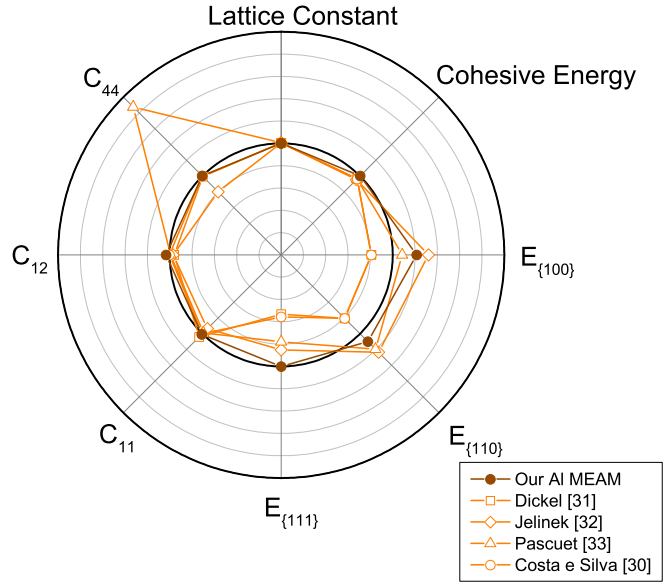

FIG. 4. Fitting error for the lattice constant, cohesive energy, surface energies, and elastic constants for our Al MEAM potential and comparison Al MEAM potentials from the literature. Circles are separated by 10% fitting error, where the thick inner circle indicates 0% error. Points closer to the center than the target indicate a negative error, whereas points farther from the center than the target indicate a positive error.

the literature MEAM potentials (open data points). As seen in Fig. 5(a), our Al MEAM captures the target DFT cohesive energy curve and is fully continuous across the extent of the energy curve, avoiding discontinuities.

Our Al MEAM potential also shows good fit to the DFT target decohesive energy curve in Fig. 5(b). The curve generated by our MEAM potential is smooth up to and including the plateau value where there is no interaction between the separated {111} planes. The plateau value, which represents the unrelaxed {111} surface energy of 0.81 $\mathrm{J\,m^{-2}}$, is consistent with the computed relaxed {111} surface energy of 0.81 $\mathrm{J\,m^{-2}}$.

As shown in Fig. 5(c), our Al MEAM potential provides decent agreement with the target DFT GSFE curve. The unstable and stable stacking fault energies produced by our Al MEAM potential are 0.175 and 0.085 $\mathrm{J\,m^{-2}}$, respectively, and compare well with the target DFT values of 0.154 and 0.106 $\mathrm{J\,m^{-2}}$. Our Al MEAM potential is also able to capture the correct shape and magnitude of the second peak at $\frac{b}{b_0} \approx \frac{2}{3}$, avoiding instabilities or local minima.

C. Cu target results

A summary of the fit error of target properties for our Cu MEAM potential are shown in Fig. 6 along with errors from the literature Cu MEAM potentials for comparison. Numerical values of these properties are given in Table S3. Our Cu MEAM potential captures the target surface energies well with absolute errors of 20.1%, 16.1%, and 16.7% for the {100}, {110}, and {111} surfaces, respectively. Our Cu MEAM potential also shows good reproduction of the elastic constants with absolute errors of −0.7%, −1.3%, and −0.1% for C_{11}, C_{12}, and C_{44}, respectively.

Figure 7 summarizes the target Cu cohesive energy, decohesive energy, and GSFE curves (target DFT data are indicated by the solid curve) along with curves produced by our MEAM potential (solid data points) and comparison with the literature MEAM potentials (open data points). As seen in Fig. 7(a), our Cu MEAM captures the target DFT cohesive energy curve and is fully continuous across the extent of the energy curve, avoiding discontinuities.

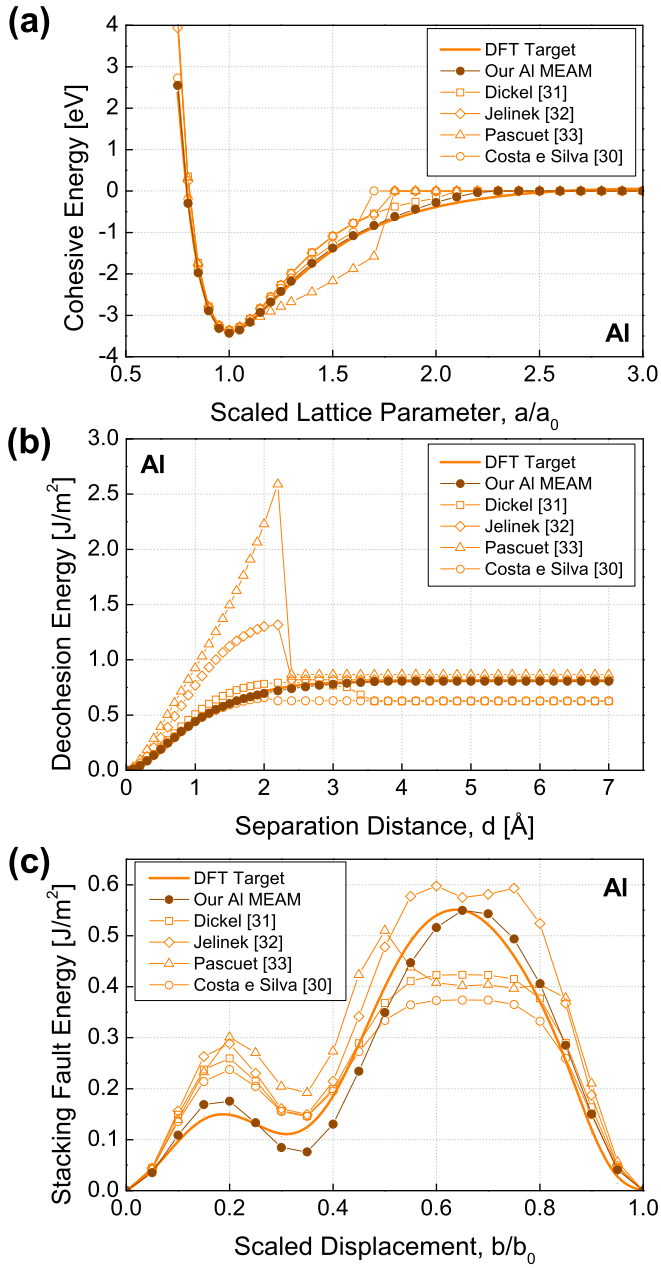

FIG. 5. Summary of target energy curves for Al (solid curves) with our Al MEAM potential (solid data points) and MEAM potentials from the literature (open data points). (a) shows the cohesive energy curve, (b) shows the decohesive energy curve, and (c) shows the GSFE curve.

Figure 7(b) shows the target decohesive energy curve for Cu along with our Cu MEAM potential. Our Cu MEAM potential shows good fit to the DFT target curve and is entirely smooth up to and including the plateau value, where there is no interaction between the separated {111} planes. The plateau value, which represents the unrelaxed {111} surface energy of 1.55 J m^{-2}, is consistent with the computed relaxed {111} surface energy of 1.54 J m^{-2}.

As shown in Fig. 7(c), our Cu MEAM potential provides good agreement with the target DFT GSFE curve. The unstable and stable stacking fault energies produced by our Cu

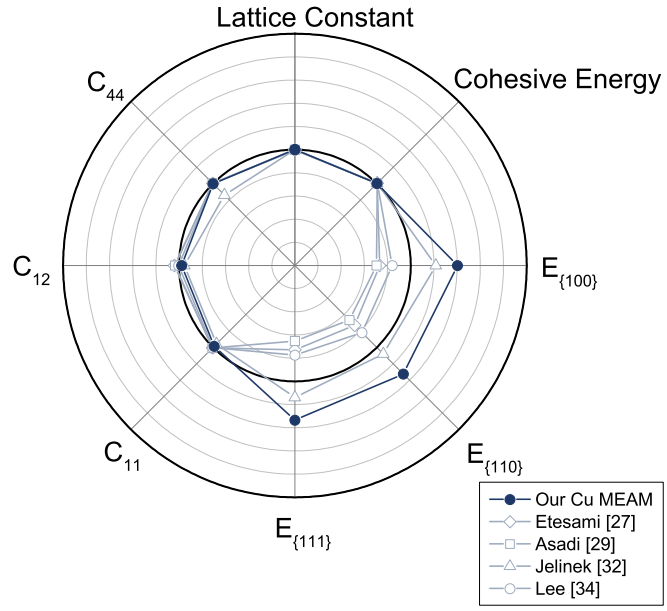

FIG. 6. Fitting error for the lattice constant, cohesive energy, surface energies, and elastic constants for our Cu MEAM potential and comparison Cu MEAM potentials from the literature. Circles are separated by 10% fitting error, where the thick inner circle indicates 0% error. Points closer to the center than the target indicate a negative error, whereas points farther from the center than the target indicate a positive error.

MEAM potential are 0.170 and 0.022 J m^{-2}, respectively. These values compare well with the same values calculated from DFT of 0.143 J m^{-2} and 0.026 J m^{-2}. Our Cu MEAM potential is also able to capture the correct shape and magnitude of the second peak at $\frac{b}{b_0} \approx \frac{2}{3}$, avoiding instabilities or local minima.

IV. TEMPERATURE DEPENDENCE OF ELASTIC CONSTANTS

In order to explore the transferability of our fcc MEAM potentials, we used them to calculate the temperature dependence of the elastic constants which were not included as fitting targets. Figure 8 provides the elastic constants as a function of temperature from 0 to 800 K with experimental data for comparison. Figure 8 demonstrates that across a wide range of temperatures, our MEAM potential predictions match well with experimental elastic constants of Ni [35], Al [36,37], and Cu [38,39].

V. DISCUSSION

Our MEAM potentials and several MEAM potentials from the literature provide reasonable agreement with experimental/*ab initio* values of relaxed surface energies and elastic constants. Inspection of the cohesive, decohesive, and GSFE energy curves in Figs. 3, 5, and 7 reveals that by including only single data point equilibrium cohesive energy, surface energies, and stable stacking fault energy as target properties, continuous curves generated using the literature potentials often display erroneous behavior.

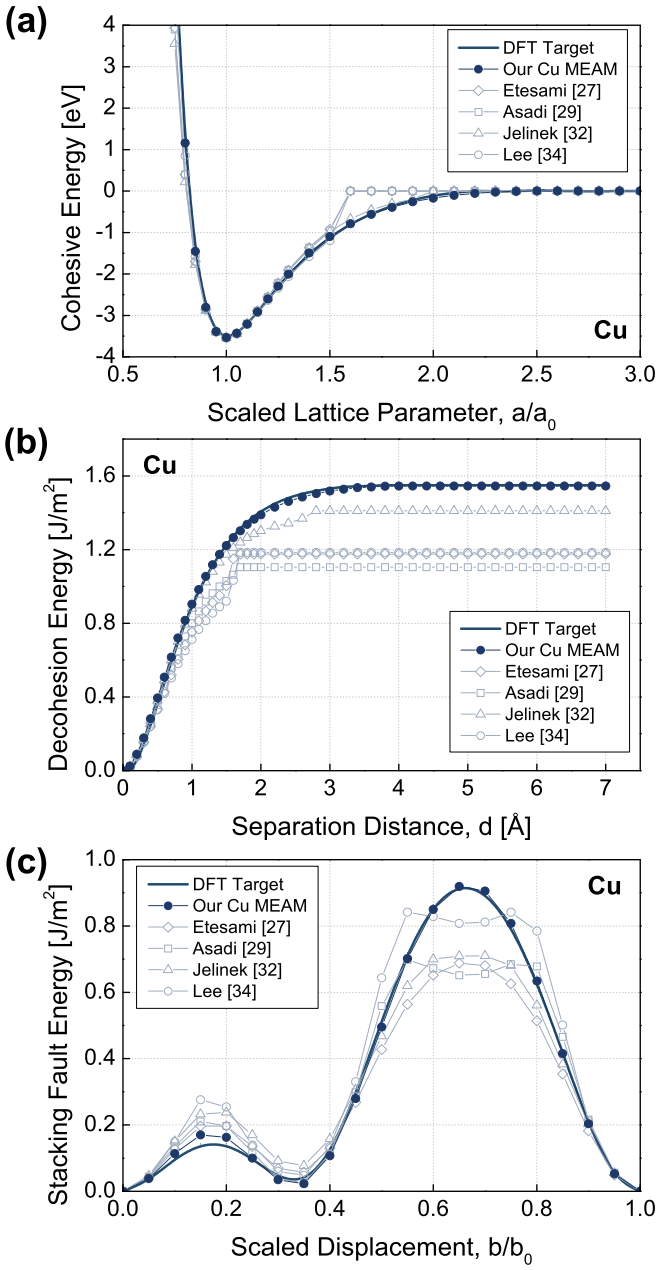

FIG. 7. Summary of target energy curves for Cu (solid curves) with our Cu MEAM potential (solid data points) and MEAM potentials from the literature (open data points). (a) shows the cohesive energy curve, (b) shows the decohesive energy curve, and (c) shows the GSFE curve.

Cohesive energy curves for our three fcc MEAM potentials and the literature potentials show good agreement near the equilibrium lattice position [Figs. 3(a), 5(a), and 7(a)]. For lattice parameter values at and above $1.5a_0$, potentials tend to deviate from the first-principles cohesive energy curve. Cohesive energy curves generated by the literature potentials show a discontinuity between $1.6a_0$ and $1.8a_0$ that is caused by the expansion beyond the cutoff radius. Such a discontinuity, which is avoided in our fcc MEAM potentials, can generate a strong, anomalous restoring force under volumetric deformations.

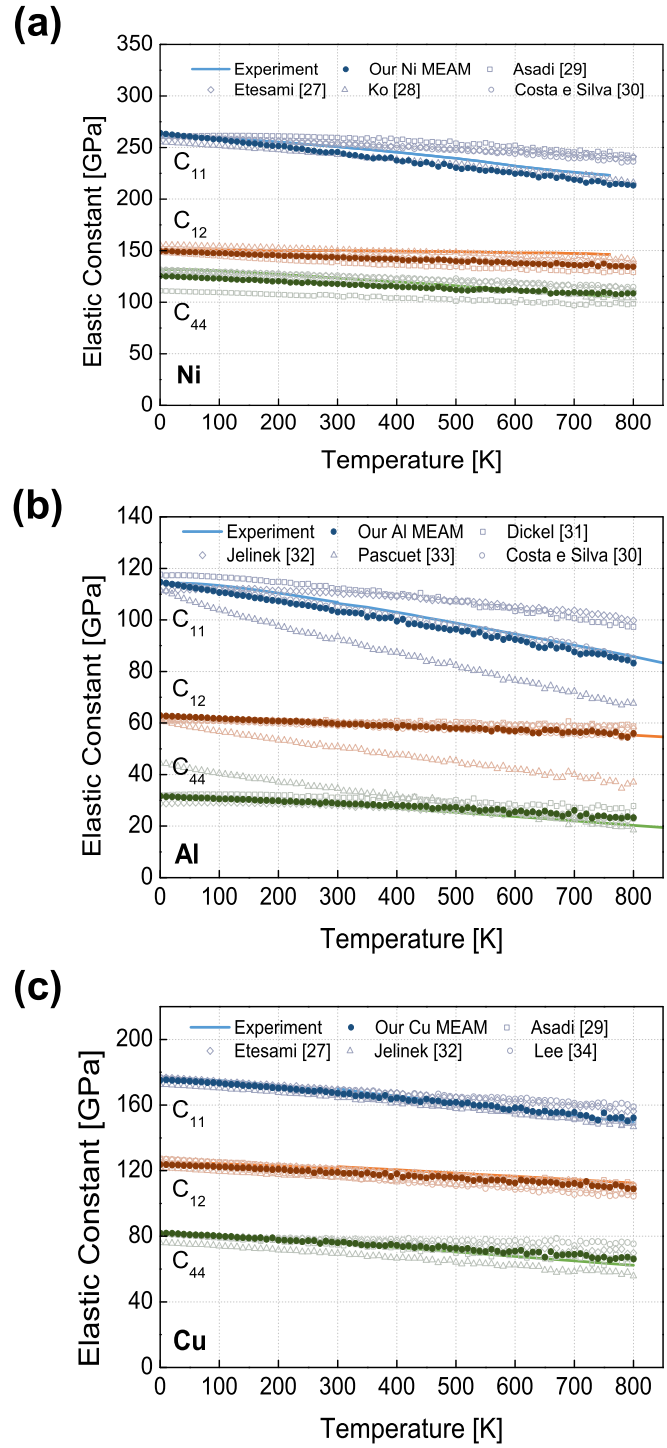

FIG. 8. Summary of predicted elastic constants as a function of temperature for (a) Ni, (b) Al, and (c) Cu. Experimental data are shown as solid curves.

Decohesive energy curves vary significantly between our MEAM potentials and the literature potentials. There are several common features among the literature potentials that differ from our MEAM potentials. Some decohesive curves, notably in Al [32,33], show significant increases in energy even at small separation distances. Such large increases are expected to generate an erroneous pressure that resists

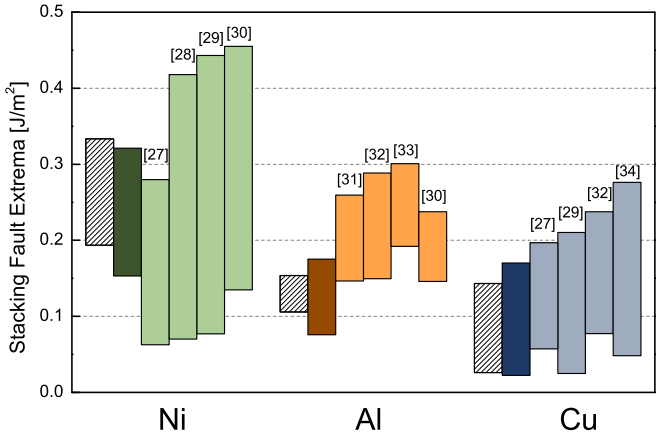

FIG. 9. Summary of the unstable (maximum of column) and stable (minimum of column) stacking fault energies for DFT targets (diagonal pattern), our FCC MEAM potentials (dark color), and MEAM potentials from the literature (light color).

fracturelike deformations. Potentials from the literature also often show discontinuities (a drop or jump in planar energy) as atoms on either surface approach the cutoff radius, which will generate anomalous forces near the cutoff distance. Such a discontinuity would manifest as a stress that actually promotes (or impedes) separation of the two planes near the cutoff radius. These discontinuities are noticeable for Ni MEAM potentials between 1.6 and 2.8 Å (79%–138% of the planar spacing of the {111} Ni planes), for Al MEAM potentials at 2.4 Å (approximately the planar spacing of the {111} Al planes), and for Cu MEAM potentials between 1.7 and 2.8 Å (81%–133% the planar spacing of the {111} Cu planes). Decohesive energy curves from the literature can also show error in the plateau surface energy in the unrelaxed free surface limit which typically corresponds to any error in the relaxed {111} surface energies.

GSFE curves also show significant differences between our MEAM potentials and the literature potentials. Differences are chiefly between the unstable and stable stacking fault energies and the secondary peak. The unstable stacking fault energy is important in contributing to the nucleation barrier of partial dislocations. The relative difference between the unstable and stable stacking fault energies has been shown to be important for the prevalence of extended partial versus full dislocations [12]. Figure 9 summarizes these features of the GSFE curves for target DFT data, our MEAM potentials, and the literature potentials. The maximum point of each column corresponds to the unstable stacking fault energy, and the minimum point of each column corresponds to the stable stacking fault energy. Figure 9 [and Figs. 3(c), 5(c), and 7(c)] shows that the literature potentials tend to overestimate the unstable stacking fault energy. It is also seen that the literature potentials for Al and Cu tend to overestimate the stable stacking fault energy, while the literature potentials for Ni all underestimate the stable stacking fault energy. Overestimation of unstable stacking fault energy in the literature potentials would lead to an error in the nucleation energy required for leading partial dislocation nucleation. Figure 9 also demonstrates that our fcc MEAM potentials provide an improved fit to the average energy level between the unstable and stable stacking fault positions. Notably, all Al MEAM potentials from the literature predict stable stacking fault energies that are similar to the unstable stacking fault energy from DFT. This demonstrates an overall increase in the GSFE landscape of these Al MEAM literature potentials which can lead to erroneously high shearing strengths in these potentials. Our Al MEAM potential shows a relative difference between the unstable and stable stacking fault energies similar to that of the literature potentials but is more accurately centered at the DFT values. Although the region between $\frac{b}{b_0} = 0.4$ and 0.8 in Figs. 3(c), 5(c), and 7(c) is not typically encountered in simulation, the shape of this second peak calculated using the literature potentials is often nonphysical, even displaying a local minimum in some of the potentials.

Figure 8 shows the predicted elastic constants C_{11}, C_{12}, and C_{44} as a function of temperature for our Ni, Al, and Cu MEAM potentials (solid data points) and also potentials from the literature (open data points). Experimental data are also included for comparison (solid curve). Our potentials match the experimental data well for Ni [35], Al [36,37], and Cu [38,39]. Notably, our potentials show a significant improvement in the prediction of the temperature dependence of C_{11} compared to most other literature potentials.

In order to investigate the ability of our MEAM potentials to predict relevant material properties not included in the training data set, we have also calculated the thermal expansion coefficient at 300 K [40–42], the equilibrium dislocation dissociation distance [43–46], and the vacancy formation energy [47–58]. The results of these calculations as well as a comparison to first-principles and experimental reference from the literature are provided for Ni (Table S4), Al (Table S5), and Cu (Table S6) in the Supplemental Material. We find that overall, the thermal expansion coefficient predicted by our MEAM potentials match well with experimental values for Ni, Al, and Cu. The equilibrium dislocation dissociation distance for both edge and screw-type dislocations of all elements appears to correlate with the stable stacking fault energies predicted by our potentials. Prediction of a stable stacking fault energy that is greater than other literature potentials tends to correspond to a dissociation distance that is shorter than that of the literature potentials, and an underprediction of the stable stacking fault energy tends to correspond to a larger dissociation distance compared to that of the literature potentials. Predictions of vacancy formation energy for Ni, Al, and Cu appear to overpredict the literature values. Compared to the average vacancy formation energy predicted from literature potentials, our MEAM potentials show a difference of 65% for Ni, 19.6% for Al, and 24.1% for Cu. We believe that these increases arise chiefly from the increased cutoff radius used in our MEAM potentials. Compared to the average cutoff radius used in the literature potentials cited here, our potentials have cutoff radii that differ by 24.5% for Ni, 25.0% for Al, and 50.7% for Cu, indicating an overall significant increase in cutoff radius for our potentials. This increased cutoff radius could lead to a significant increase in atomic interactions among atoms surrounding the vacancy, leading to higher formation energy values. In previous potentials, the lower cutoff radius was chosen for computational efficiency. We have shown here that for many properties

relevant for mechanical behavior such as fracture and plasticity, an increased cutoff radius results in a more accurate fitting, suggesting that is most appropriate for our application.

We have demonstrated how our fitting approach can yield improved accuracy compared to existing empirical potentials. It should be noted that all potentials (including MEAM potentials) contain trade-offs in accuracy, transferability, and computational cost. Classical empirical potentials are typically formulated by assuming specific underlying physics of the atomic interactions. Where these formulations are not sufficient, new classes of potentials have the possibility to provide improvements. Along with empirical potentials such as EAM and MEAM, machine learning (ML) potentials have also shown success in modeling metallic fcc [59] and bcc systems across a broad composition range [60] and have demonstrated success in modeling semiconductor materials [59–63]. Compared to more classical potentials, ML potentials are often significantly more computationally expensive, but they often exhibit improved accuracy comparable to first-principles calculations [61].

ML potentials can be categorized through their choice of local atomic environment descriptor and ML model. Different combinations of these components have given rise to the neural network potential [64], the Gaussian approximation potential [65,66], the spectral neighbor analysis potential [67], and the moment tensor potential [68,69]. Such potentials are trained on a large data set that is typically generated from DFT simulation. Considering transferability, empirical potentials are typically formulated based on underlying physics, which can act to constrain their applicability to specific chemistries. Although it should be noted that any interatomic potential is biased towards its training data set, ML potentials may have the flexibility to cover a broader range of chemistries and phases [61]. Efforts have also been put towards modularizing ML potentials, which allows the construction of alloy-type potentials without requiring retraining [63]. As a more recent class of interatomic potentials, ML potentials are currently less widely used, although the accessibility of ML potentials has continued to increase with several open-source training platforms available in the literature [62,63]. With broader adoption, systems and simulations that benefit the most from ML potentials will surely become more apparent. We may even imagine a hybrid-type approach that includes components of empirical potentials and ML potentials. This would ideally combine the efficiency and motivating physics of empirical potentials with the accuracy of the ML methods.

VI. CONCLUSION

Here we have presented Ni, Al, and Cu MEAM potentials that are able to capture properties relevant to plastic deformation and fracture processes in these metals. In doing so, beyond using a single data point to represent the fitting target, we have incorporated the cohesive energy curve, decohesive energy curve, and full generalized stacking fault energy curve that govern key continuous mechanistic processes in fracture and plasticity as the fitting targets. We have demonstrated, indeed, that such a strategy leads to the overall improvement in capturing the cohesive energy curve, decohesive energy curve, and GSFE curve, leading to an improvement in describing the plasticity and fracture behaviors. We have also demonstrated that overall, our MEAM potentials outperform all existing MEAM potentials readily available from the literature. Due to the overall much improved predictability, it is expected that these MEAM potentials will be widely used to simulate the plastic deformation and fracture processes in unary fcc metals.

ACKNOWLEDGMENTS

The support from the Agency for Science, Technology and Research (A*STAR) under Grant No. AMDM A1898b0043 and the use of computing resources at the A*STAR Computational Resource Centre and National Supercomputer Centre, Singapore, are gratefully acknowledged.

[1] Z. H. Aitken, V. Sorkin, and Y.-W. Zhang, Atomistic modeling of nanoscale plasticity in high-entropy alloys, J. Mater. Res. **34**, 1509 (2019).

[2] Z. Wu and W. A. Curtin, The origins of high hardening and low ductility in magnesium, Nature (London) **526**, 62 (2015).

[3] Z. Wu, R. Ahmad, B. Yin, S. Sandlöbes, and W. A. Curtin, Mechanistic origin and prediction of enhanced ductility in magnesium alloys, Science **359**, 447 (2018).

[4] M. S. Daw and M. I. Baskes, Embedded-atom method: Derivation and application to impurities, surfaces, and other defects in metals, Phys. Rev. B **29**, 6443 (1984).

[5] S. M. Foiles, M. I. Baskes, and M. S. Daw, Embedded-atom-method functions for the fcc metals Cu, Ag, Au, Ni, Pd, Pt, and their alloys, Phys. Rev. B **33**, 7983 (1986).

[6] M. I. Baskes, Modified embedded-atom potentials for cubic materials and impurities, Phys. Rev. B **46**, 2727 (1992).

[7] B.-J. Lee, M. I. Baskes, H. Kim, and Y. K. Cho, Second nearest-neighbor modified embedded atom method potentials for bcc transition metals, Phys. Rev. B **64**, 184102 (2001).

[8] B.-J. Lee, J.-H. Shim, and M. I. Baskes, Semiempirical atomic potentials for the fcc metals Cu, Ag, Au, Ni, Pd, Pt, Al, and Pb based on first and second nearest-neighbor modified embedded atom method, Phys. Rev. B **68**, 144112 (2003).

[9] W.-M. Choi, Y. Kim, D. Seol, and B.-J. Lee, Modified embedded-atom method interatomic potentials for the Co-Cr, Co-Fe, Co-Mn, Cr-Mn and Mn-Ni binary systems, Comput. Mater. Sci. **130**, 121 (2017).

[10] C. Wu, B.-J. Lee, and X. Su, Modified embedded-atom interatomic potential for Fe-Ni, Cr-Ni and Fe-Cr-Ni systems, CALPHAD: Comput. Coupling Phase Diagrams Thermochem. **57**, 98 (2017).

[11] Y.-K. Kim, W.-S. Jung, and B.-J. Lee, Modified embedded-atom method interatomic potentials for the Ni–Co binary and the Ni–Al–Co ternary systems, Modell. Simul. Mater. Sci. Eng. **23**, 055004 (2015).

[12] H. Van Swygenhoven, P. M. Derlet, and A. G. Frøseth, Stacking fault energies and slip in nanocrystalline metals, Nat. Mater. **3**, 399 (2004).

[13] Z. Wu, M. F. Francis, and W. A. Curtin, Magnesium interatomic potential for simulating plasticity and fracture phenomena, Modell. Simul. Mater. Sci. Eng. **23**, 015004 (2015).

[14] A. A. Griffith, The phenomena of rupture and flow in solids, Phil. Trans. Royal Soc. A. **221**, 163 (1921).

[15] J. A. Zimmerman, H. Gao, and F. F. Abraham, Generalized stacking fault energies for embedded atom FCC metals, Modell. Simul. Mater. Sci. Eng. **8**, 103 (2000).

[16] J. P. Perdew, K. Burke, and M. Ernzerhof, Generalized Gradient Approximation Made Simple, Phys. Rev. Lett. **77**, 3865 (1996).

[17] P. E. Blöchl, Projector augmented-wave method, Phys. Rev. B **50**, 17953 (1994).

[18] G. Kresse and J. Furthmüller, Efficient iterative schemes for *ab initio* total-energy calculations using a plane-wave basis set, Phys. Rev. B **54**, 11169 (1996).

[19] H. J. Monkhorst and J. D. Pack, Special points for Brillouin-zone integrations, Phys. Rev. B **13**, 5188 (1976).

[20] M. Methfessel and A. T. Paxton, High-precision sampling for Brillouin-zone integration in metals, Phys. Rev. B **40**, 3616 (1989).

[21] D. J. Chadi and M. L. Cohen, Special points in the Brillouin zone, Phys. Rev. B **8**, 5747 (1973).

[22] A. Hjorth Larsen *et al.*, The atomic simulation environment—A Python library for working with atoms, J. Phys.: Condens. Matter **29**, 273002 (2017).

[23] S. Bahn and K. Jacobsen, An object-oriented scripting interface to a legacy electronic structure code, Comput. Sci. Eng. **4**, 56 (2002).

[24] See Supplemental Material at http://link.aps.org/supplemental/10.1103/PhysRevB.103.094116 for methodology description and additional property calculations.

[25] S. Plimpton, Fast parallel algorithms for short-range molecular dynamics, J. Comput. Phys. **117**, 1 (1995).

[26] J. H. Rose, J. Ferrante, and J. R. Smith, Universal Binding Energy Curves for Metals and Bimetallic Interfaces, Phys. Rev. Lett. **47**, 675 (1981).

[27] S. A. Etesami and E. Asadi, Molecular dynamics for near melting temperatures simulations of metals using modified embedded-atom method, J. Phys. Chem. Solids **112**, 61 (2018).

[28] W.-S. Ko, B. Grabowski, and J. Neugebauer, Development and application of a Ni-Ti interatomic potential with high predictive accuracy of the martensitic phase transition, Phys. Rev. B **92**, 134107 (2015).

[29] E. Asadi, M. Asle Zaeem, S. Nouranian, and M. I. Baskes, Two-phase solid–liquid coexistence of Ni, Cu, and Al by molecular dynamics simulations using the modified embedded-atom method, Acta Mater. **86**, 169 (2015).

[30] A. Costa e Silva, J. Ågren, M. T. Clavaguera-Mora, D. Djurovic, T. Gomez-Acebo, B.-J. Lee, Z.-K. Liu, P. Miodownik, and H. J. Seifert, Applications of computational thermodynamics – The extension from phase equilibrium to phase transformations and other properties, CALPHAD: Comput. Coupling Phase Diagrams Thermochem. **31**, 53 (2007).

[31] D. E. Dickel, M. I. Baskes, I. Aslam, and C. D. Barrett, New interatomic potential for Mg–Al–Zn alloys with specific application to dilute Mg-based alloys, Modell. Simul. Mater. Sci. Eng. **26**, 045010 (2018).

[32] B. Jelinek, S. Groh, M. F. Horstemeyer, J. Houze, S. G. Kim, G. J. Wagner, A. Moitra, and M. I. Baskes, Modified embedded atom method potential for Al, Si, Mg, Cu, and Fe alloys, Phys. Rev. B **85**, 245102 (2012).

[33] M. Pascuet and J. Fernández, Atomic interaction of the MEAM type for the study of intermetallics in the Al–U alloy, J. Nucl. Mater. **467**, 229 (2015).

[34] B.-J. Lee, B. D. Wirth, J.-H. Shim, J. Kwon, S. C. Kwon, and J.-H. Hong, Modified embedded-atom method interatomic potential for the Fe-Cu alloy system and cascade simulations on pure Fe and Fe-Cu alloys, Phys. Rev. B **71**, 184205 (2005).

[35] G. Alers, J. Neighbours, and H. Sato, Temperature dependent magnetic contributions to the high field elastic constants of nickel and an Fe-Ni alloy, J. Phys. Chem. Solids **13**, 40 (1960).

[36] D. Gerlich and E. Fisher, The high temperature elastic moduli of aluminum, J. Phys. Chem. Solids **30**, 1197 (1969).

[37] G. N. Kamm and G. A. Alers, Low-temperature elastic moduli of aluminum, J. Appl. Phys. **35**, 327 (1964).

[38] W. C. Overton and J. Gaffney, Temperature variation of the elastic constants of cubic elements. I. Copper, Phys. Rev. **98**, 969 (1955).

[39] Y. A. Chang and L. Himmel, Temperature dependence of the elastic constants of Cu, Ag, and Au above room temperature, J. Appl. Phys. **37**, 3567 (1966).

[40] F. C. Nix and D. MacNair, The thermal expansion of pure metals: Copper, gold, aluminum, nickel, and iron, Phys. Rev. **60**, 597 (1941).

[41] F. R. Kroeger and C. A. Swenson, Absolute linear thermal-expansion measurements on copper and aluminum from 5 to 320 K, J. Appl. Phys. **48**, 853 (1977).

[42] R. H. Carr, R. D. McCammon, and G. K. White, The thermal expansion of copper at low temperatures, Proc. R. Soc. London, Ser. A **280**, 72 (1964).

[43] C. B. Carter and S. M. Holmes, The stacking-fault energy of nickel, Philos. Mag. **35**, 1161 (1977).

[44] C. Woodward, D. R. Trinkle, L. G. Hector, and D. L. Olmsted, Prediction of Dislocation Cores in Aluminum from Density Functional Theory, Phys. Rev. Lett. **100**, 045507 (2008).

[45] D. J. H. Cockayne, M. L. Jenkins, and I. L. F. Ray, The measurement of stacking-fault energies of pure face-centred cubic metals, Philos. Mag. **24**, 1383 (1971).

[46] W. M. Stobbs and C. H. Sworn, The weak beam technique as applied to the determination of the stacking-fault energy of copper, Philos. Mag. **24**, 1365 (1971).

[47] P. A. Korzhavyi, I. A. Abrikosov, B. Johansson, A. V. Ruban, and H. L. Skriver, First-principles calculations of the vacancy formation energy in transition and noble metals, Phys. Rev. B **59**, 11693 (1999).

[48] H. Matter, J. Winter, and W. Triftshäuser, Phase transformations and vacancy formation energies of transition metals by positron annihilation, Appl. Phys. **20**, 135 (1979).

[49] J. Wolff, M. Franz, J.-E. Kluin, and D. Schmid, Vacancy formation in nickel and α-nickel-carbon alloy, Acta Mater. **45**, 4759 (1997).

[50] J. L. Campbell, C. S. Schulte, and J. A. Jackman, Temperature dependence of positron trapping in silver and nickel, J. Phys. F **7**, 1985 (1977).

[51] M. J. Gillan, Calculation of the vacancy formation energy in aluminium, J. Phys.: Condens. Matter **1**, 689 (1989).

[52] W. Triftshäuser, Positron trapping in solid and liquid metals, Phys. Rev. B **12**, 4634 (1975).

[53] A. Berger, S. Ockers, M. Chason, and R. Siegel, A study of vacancy-iron interactions in quenched aluminum, J. Nucl. Mater. **69–70**, 734 (1978).

[54] M. J. Fluss, L. C. Smedskjaer, M. K. Chason, D. G. Legnini, and R. W. Siegel, Measurements of the vacancy formation enthalpy in aluminum using positron annihilation spectroscopy, Phys. Rev. B **17**, 3444 (1978).

[55] R. R. Bourassa and B. Lengeler, The formation and migration energies of vacancies in quenched copper, J. Phys. F **6**, 1405 (1976).

[56] J. McGervey and W. Triftshäuser, Vacancy-formation energies in copper and silver from positron annihilation, Phys. Lett. A **44**, 53 (1973).

[57] C. Meechan and R. Eggleston, Formation energies of vacancies in copper and gold, Acta Metall. **2**, 680 (1954).

[58] D. A. Andersson and S. I. Simak, Monovacancy and divacancy formation and migration in copper: A first-principles theory, Phys. Rev. B **70**, 115108 (2004).

[59] J. S. Smith, B. Nebgen, N. Mathew, J. Chen, N. Lubbers, L. Burakovsky, S. Tretiak, H. A. Nam, T. Germann, S. Fensin, and K. Barros, Automated discovery of a robust interatomic potential for aluminum, arXiv:2003.04934.

[60] W. Jiang, Y. Zhang, L. Zhang, and H. Wang, Accurate deep potential model for the Al-Cu-Mg alloy in the full concentration space, arXiv:2008.11795.

[61] Y. Zuo, C. Chen, X. Li, Z. Deng, Y. Chen, J. Behler, G. Csányi, A. V. Shapeev, A. P. Thompson, M. A. Wood, and S. P. Ong, Performance and cost assessment of machine learning interatomic potentials, J. Phys. Chem. A **124**, 731 (2020).

[62] Y. Zhang, H. Wang, W. Chen, J. Zeng, L. Zhang, H. Wang, and W. E, DP-GEN: A concurrent learning platform for the generation of reliable deep learning based potential energy models, Comput. Phys. Commun. **253**, 107206 (2020).

[63] L. Zhang, D.-Y. Lin, H. Wang, R. Car, and W. E, Active learning of uniformly accurate interatomic potentials for materials simulation, Phys. Rev. Materials **3**, 023804 (2019).

[64] J. Behler, Representing potential energy surfaces by high-dimensional neural network potentials, J. Phys.: Condens. Matter **26**, 183001 (2014).

[65] A. P. Bartók, M. C. Payne, R. Kondor, and G. Csányi, Gaussian Approximation Potentials: The Accuracy of Quantum Mechanics, without the Electrons, Phys. Rev. Lett. **104**, 136403 (2010).

[66] A. P. Bartók and G. Csányi, Gaussian approximation potentials: A brief tutorial introduction, Int. J. Quantum Chem. **115**, 1051 (2015).

[67] A. Thompson, L. Swiler, C. Trott, S. Foiles, and G. Tucker, Spectral neighbor analysis method for automated generation of quantum-accurate interatomic potentials, J. Comput. Phys. **285**, 316 (2015).

[68] A. V. Shapeev, Moment tensor potentials: A class of systematically improvable interatomic potentials, Multiscale Model. Simul. **14**, 1153 (2016).

[69] E. V. Podryabinkin and A. V. Shapeev, Active learning of linearly parametrized interatomic potentials, Comput. Mater. Sci. **140**, 171 (2017).